Charge Transport Hot Paper

How to cite:
International Edition: doi.org/10.1002/anie.202217238
German Edition: doi.org/10.1002/ange.202217238

Giant Tunability of Charge Transport in 2D Inorganic Molecular Crystals by Pressure Engineering

Xin Feng[+], Kejun Bu[+], Teng Liu, Songhao Guo, Zongdong Sun, Tonghuan Fu, Yongshan Xu, Kailang Liu, Sijie Yang, Yinghe Zhao, Huiqiao Li, Xujie Lü, and Tianyou Zhai**

HPSTAR 1597-2022

Abstract: The unique intermolecular van der Waals force in emerging two-dimensional inorganic molecular crystals (2DIMCs) endows them with highly tunable structures and properties upon applying external stimuli. Using high pressure to modulate the intermolecular bonding, here we reveal the highly tunable charge transport behavior in 2DIMCs for the first time, from an insulator to a semiconductor. As pressure increases, 2D α-Sb_2O_3 molecular crystal undergoes three isostructural transitions, and the intermolecular bonding enhances gradually, which results in a considerably decreased band gap by 25% and a greatly enhanced charge transport. Impressively, the in situ resistivity measurement of the α-Sb_2O_3 flake shows a sharp drop by 5 orders of magnitude in 0–3.2 GPa. This work sheds new light on the manipulation of charge transport in 2DIMCs and is of great significance for promoting the fundamental understanding and potential applications of 2DIMCs in advanced modern technologies.

Introduction

Two-dimensional inorganic molecular crystals (2DIMCs) have emerged as rising stars due to their unique structure and exceptional physical properties, including long-range molecular ordering, diverse molecular structure, excellent dielectric property, and high thermal stability.[1] Unfortunately, due to the weak intermolecular coupling, they typically show poor charge transport and behave as insulators, severely hindering their potential applications in electronics and optoelectronics.[1b,2] Their intrinsic poor charge transport property is promising to be addressed by applying compressive strain.[3] Strain engineering has been known as a desirable approach to modifying the physical and chemical properties of various materials, which exhibits the powerful capability to regulate lattice structure on the atomic and molecular scale.[3,4] To date, strain-induced changes of various physical properties, such as enhanced carrier mobilities and light emission, reduced in-plane symmetry, and weakened interlayer coupling, have been widely achieved in 2D atomic crystals via changing the bond lengths and bond angle.[4b,5] Recently, strain engineering has also been applied to 2D organic molecular crystals to reinforce the intermolecular coupling by shortening the intermolecular distances.[3,4,6] A prominent example is the 6,13-bis(triisopropylsilylethynyl) pentacene (TIPS-PEN) molecular crystal, in which the hole mobility increased by 20 times under a compressive strain of 16.7%.[6b]

It should be emphasized that here, 2DIMCs possess unique structural features and are distinct from 2D atomic crystals as well as 2D organic molecular crystals.[1a,b,e] For 2D atomic crystals, each layer is formed by atoms, which are connected by strong covalent bonds; whereas in 2DIMCs, each layer is composed of inorganic molecules, which are bonded together through weak van der Waals (vdW) force.[1e] On the other hand, though 2D inorganic and organic molecular crystals are both composed of molecules, molecular volumes of inorganic molecules consisting of only a few atoms are much smaller than those of common aromatic organic molecules.[7] Besides, the unique π-π stacking in 2D organic molecular crystals, providing paths for charge hopping between neighboring molecules, is also absent in 2DIMCs.[7a,8] These huge structural differences result in the classical band transport model that is applicable for 2D atomic crystals failing to describe the charge transport behavior in 2DIMCs. Besides, whether the widely accepted transient localization theory in organic molecular crystals is applicable to 2DIMCs remains unclear yet.[8,9] With these regards, it is believed that the changes of physical property, especially the charge transport, in 2DIMCs under compression will be different from both 2D atomic crystals and 2D organic molecular crystals. Elucidating the variations of structures and properties opens fascinating opportunities to acquire emergent properties and reveal new mechanisms, but experimental research is lacking until now.

[*] X. Feng,[+] T. Liu, Z. Sun, Y. Xu, Dr. K. Liu, Dr. S. Yang, Dr. Y. Zhao, Prof. H. Li, Prof. T. Zhai
State Key Laboratory of Materials Processing and Die & Mould Technology, and School of Materials Science and Engineering, Huazhong University of Science and Technology
Wuhan 430074 (P. R. China)
E-mail: zhaity@hust.edu.cn

Dr. K. Bu,[+] S. Guo, T. Fu, Prof. L. Lü
Center for High Pressure Science and Technology Advanced Research (HPSTAR)
Shanghai 201203 (P. R. China)
E-mail: xujie.lu@hpstar.ac.cn

[+] These authors contributed equally to this work.

In this work, by using high-pressure regulation and in situ characterizations, we present the highly tunable charge transport behavior in 2D α-Sb_2O_3 inorganic molecular crystals, from insulator to a wide-band gap semiconductor. The structure changes under compression are revealed by in situ high-pressure Raman spectroscopy and DFT calculations, demonstrating that there are three isostructural transitions at ~4 GPa, 10 GPa, and 15 GPa, respectively. Besides, the transition pressures of the isostructural transitions can be tailored by regulating the crystal thickness. Bond order and electron localization function (ELF) are employed to assess the evolutions of intermolecular bonding. Upon compression, the intermolecular bonding enhances significantly, which plays an essential role in the decrease of α-Sb_2O_3 band gap and the improvement of charge transport property. Nevertheless, the nature of the indirect band gap is preserved and there is no formation of the intermolecular covalent bond up to 15 GPa. Intriguingly, a steep decrease in resistivity by 5 orders of magnitude was observed in 0–3.2 GPa, suggesting the transformation from an insulator to a semiconductor. The achievement of this work sets a new milestone for 2DIMCs and will greatly stimulate the fundamental research and potential applications of 2DIMCs in optoelectronics and nano-electromechanical systems.

Results and Discussion

The Sb_2O_3 solid includes three phases, α-Sb_2O_3, β-Sb_2O_3, and γ-Sb_2O_3. Among these three phases, α-Sb_2O_3 is a molecular crystal (space group $Fd\bar{3}m$) composed of the Sb_4O_6 molecular cage with T_d point group symmetry,[10] as depicted in Figure 1a. Given the characteristic of molecular crystal and good thermal stability of α-Sb_2O_3,[11] vertical micro-spacing sublimation (VMS) strategy (Figure 1b) was utilized to grow 2D α-Sb_2O_3 flakes, which possesses the advantages of low-cost, simple operation and short growth time in comparison with the conventional chemical vapor deposition (CVD) methods.[1b,12] Detailed growth method is provided in the section of experiment details in the Supporting Information. Typical optical microscope (OM) images of the as-synthesized α-Sb_2O_3 flakes with different sizes and thicknesses are presented in Figure S1. Monolayer α-Sb_2O_3 flake exhibits a thickness of ~0.64 nm.[1b] Significantly, the ultrathin α-Sb_2O_3 flakes below 5 nm can be also obtained in this way (Figure 1c and Figure S2), which correspond to 4 layers and 6 layers of α-Sb_2O_3, respectively.

To identify structural information of the Sb_2O_3 flakes, X-ray diffraction (XRD) and Raman spectroscopy were performed. As shown in Figure S3, the three sharp diffraction peaks can be distinguished clearly and match well with the standard cubic α-Sb_2O_3 (PDF# 05-0534), corresponding to the (111), (222), and (444) lattice planes, respectively. Raman spectroscopy, i.e., Raman active phonon modes, can be regarded as the fingerprint of a material and is an effective tool for phase identification. Figure 1d presents the Raman spectra of the as-grown Sb_2O_3 flakes at ambient pressure ranging from 50 to 500 cm^{-1} and the peak positions of the six Raman peaks are consistent with the data of α-Sb_2O_3 in previous reports.[12a,13] Among the six peaks, the F_{2g} located at 84 cm^{-1} is the translational mode (intermolecular vibration) and the rest are internal modes (intramolecular vibrations). Moreover, transmission electron microscopy (TEM) was utilized to further illustrate the high quality and crystalline phases of Sb_2O_3 flakes. The Sb_2O_3 flakes on mica

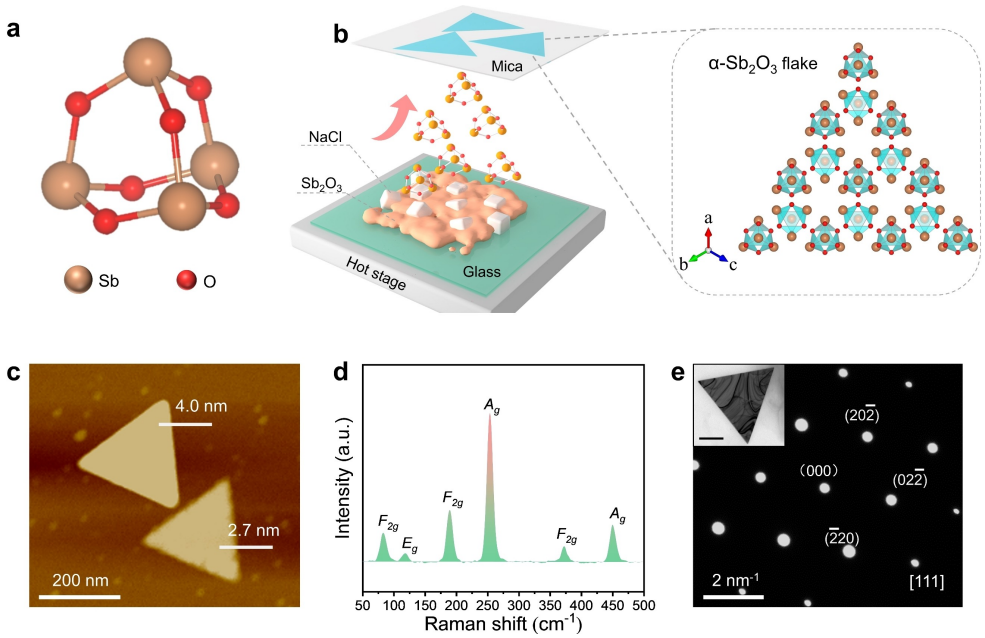

Figure 1. VMS growth and characterizations of ultrathin single-crystalline α-Sb_2O_3 flakes. a) Structural diagram of the Sb_4O_6 molecule. b) The schematic diagram for the growth process. c) AFM image of the as-synthesized α-Sb_2O_3 flakes. d) Raman spectra of the α-Sb_2O_3 flakes. e) SAED pattern of the α-Sb_2O_3 flake. Inset: TEM image with a scale bar of 2 μm.

were transferred onto the TEM Cu grid with carbon film via a PMMA-assisted method.[1b] The selected area electron diffraction (SAED) pattern in Figure 1e shows distinct hexagonal diffraction spots, indicating that the Sb_2O_3 flakes are high-quality single crystals. The calculated interplanar spacing from the SAED pattern is about 4.0 Å, in good accordance with the interplanar distance of $(\bar{2}20)$ plane in α-Sb_2O_3.[14] The chemical composition of Sb_2O_3 flakes was also verified by energy-dispersive X-ray spectroscopy (EDS). As illustrated in Figure S4a, only Sb and O elements can be detected and the Sb and O elements are uniformly distributed (Figure S4b,c) across the whole flake, demonstrating the chemical uniformity of the nanoflake. The above characterizations reveal the high crystal quality of as-grown α-Sb_2O_3 flakes, which is the basis for the following research.

Pressure serves as a fundamental thermodynamic variable that has been widely used to create novel structures and modify the properties of functional materials.[4c,15] For example, the $Cs_2AgBiBr_6$ and $Cs_2PbI_2Cl_2$ show large band-narrowing of 22.3 %, and significant photocurrent enhancement under high pressure, respectively.[15a,16] To reveal the structural changes during compression, Raman spectra of α-Sb_2O_3 flakes with pressure increasing were recorded using a symmetrical diamond anvil cell (DAC). Raman spectra provide a wealth of information for the phonons, which can be used to investigate chemical bonds, intermolecular forces, and structural features of molecular crystals.[17] Figure 2a presents the process of loading α-Sb_2O_3 flake into the DAC chamber. We first measured the pressure-dependent Raman spectra of an α-Sb_2O_3 flake with a thickness of 345 nm (Figure S5). The three additional Raman peaks in Figure S5 can be attributed to the mica substrate, as confirmed by Figure S6. The evolutions of Raman peak positions of this α-Sb_2O_3 flake are summarized in Figure 2b–e. The translational mode F_{2g} (external mode) at 89.5 cm^{-1} shifts to higher wave numbers (blue-shift) from ambient pressure to 3.77 GPa (Figure 2b) and disappears at higher pressure. Meanwhile, we noticed that the pressure coefficient of the A_g mode (255 cm^{-1}) changes at ~3 GPa, 11 GPa, and 16 GPa. The E_g mode (120 cm^{-1}) changes the slope of pressure dependence at 4 GPa and 15 GPa. Besides, the F_{2g} mode (364 cm^{-1}) also changes its slope of pressure dependence at 3.5 GPa and 10 GPa. The evolution of Raman frequency with pressure is caused by the anharmonic part as the stiffness coefficient of chemical bonds changes with the interatomic distance upon compression.[17b] According to the Grüneisen scaling approximation, the slope of Raman frequency under pressure can be deduced as $d\omega_i/dP = \kappa\gamma_i\omega_{i(0)}$, where $\omega_{i(0)}$ denotes the zero-pressure frequency of the Raman mode ω_i.[17a,18] Isothermal compressibility κ is mainly affected by the strength of the chemical bonds and crystal structure.[13a,19] Mode-Grüneisen parameter γ_i is determined by the bond stiffness-bond strain relation.[17a] Based on the above discussions, the variations of pressure coefficient for these Raman modes can be attributed to the changes of isothermal compressibility κ or mode-Grüneisen parameter,[17a,18] which signify the changes in the crystal structure or chemical bond properties at around 4 GPa, 10 GPa and 15 GPa. Therefore, it is concluded that there are three structural transitions from 0 to 22 GPa, which appear at ~4 GPa, ~10 GPa, and ~15 GPa, respectively. Besides, the three structural transitions are

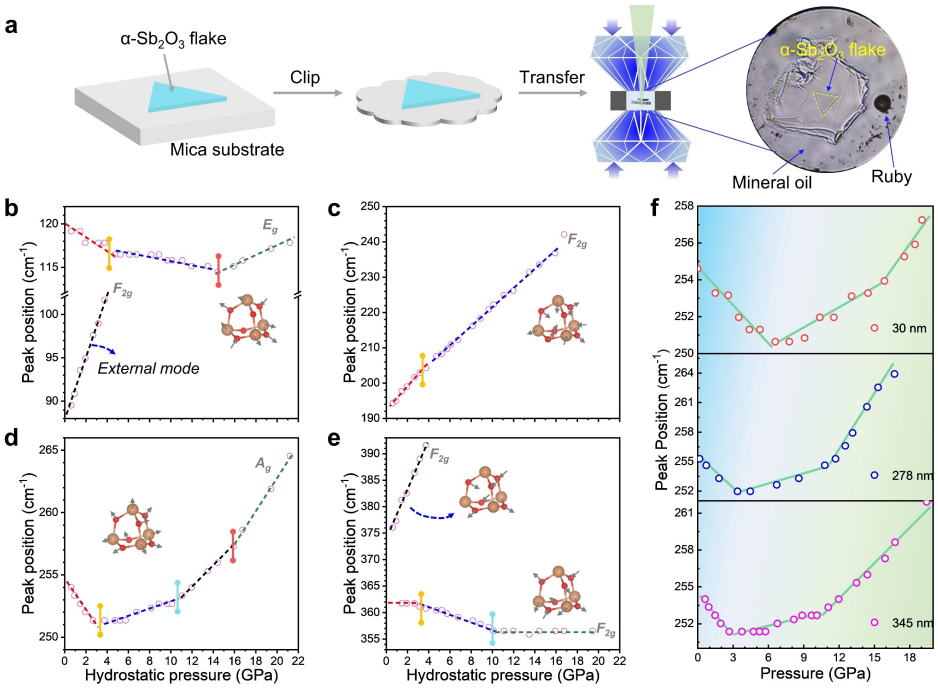

Figure 2. In situ high-pressure Raman measurements for the α-Sb_2O_3 flake. a) The process for loading α-Sb_2O_3 flake into the DAC chamber. b–e) Pressure dependence of Raman peak positions of the α-Sb_2O_3 flake. Insets are schematic diagrams of the corresponding vibration modes.[11,14b] f) Pressure dependence of the A_g mode (255 cm^{-1}) peak position in α-Sb_2O_3 flakes with different thicknesses.

reversible (as confirmed by Figure S7). Given the absence of new Raman peaks that may be related to the four possible high-pressure phases of α-Sb_2O_3 during 0–20 GPa, we infer that the three structural transitions are all isostructural phase transformations.[13]

Another distinctive feature is that the E_g (120 cm^{-1}), A_g (255 cm^{-1}), and F_{2g} (362 cm^{-1}) modes shift to lower wavenumbers (red shift) at relatively low pressure (Figure 2b,d,e). The red shift of Raman peak positions with pressure (phonon softening) is abnormal as it is usually associated with lattice expansion.[20] Given the cubic symmetry of α-Sb_2O_3, it is impossible that the lattice of α-Sb_2O_3 expands with pressure. Seeing that the E_g (120 cm^{-1}), A_g (255 cm^{-1}), and F_{2g} (362 cm^{-1}) modes belong to the intramolecular vibrations, we argue that the red-shift of the three Raman modes is probably related to the softening of intramolecular covalent bonds, which isn't included in the three change types (i.e., bond shortening, bond-angle bending, and intermolecular compression), as summarized by M. Hazen and Larry W. Finger in 1985.[21]

To reveal the effect of flake thickness on the above-mentioned structure changes, pressure-dependent Raman spectra of the other two α-Sb_2O_3 nanoflakes with thicknesses of 278 nm and 30 nm were measured (Figure S8). Figure 2f displays the evolution of the A_g mode (255 cm^{-1}) with pressure for the three α-Sb_2O_3 flakes. Since A_g mode (255 cm^{-1}) is less sensitive to the third structural transition, here we shall mainly focus on the first two structural transitions. As the thickness of α-Sb_2O_3 nanoflake decreases, the first two isostructural transitions are delayed considerably. Besides, the slope of the A_g mode (255 cm^{-1}) also diminishes with the decrease in thickness from ambient pressure to where the first structural transition occurs. These influences that seem to be caused by the thickness variation may arise from the interfacial adhesion force between the mica substrate and α-Sb_2O_3 nanoflakes, which induces the existence of deviatoric stress, thus breaking the quasi-hydrostatic condition.[22] This result inspires us that we can regulate the compression behavior of 2DIMCs by adhesion force design via changing the substrate and sample thickness.

To clarify the microscopic structural changes on the atomic level during compression, we carried out density functional theory (DFT) calculations on the high-pressure structures of α-Sb_2O_3 by employing Grimme's DFT-D3 correction method.[23] Figure 3a shows the calculated unit-cell volume as a function of pressure. Based on these three isostructural transitions, the *P-V* data were fitted in four regions using second-order Birch-Murnaghan state equations.[24] The bulk modulus B_0 for the four regions (0–4 GPa, 4–10 GPa, 10–15 GPa, and 15–28 GPa) are determined to be 22.0(3), 38.1(4), 52.4(8), and 64.1(3) GPa, respectively. The relatively small B_0 in 0–4 GPa indicates the highly compressible feature of molecular crystals. In the meantime, we reveal that the possible phase transition to tetragonal phase Sb_2O_3 proposed by Zhao et al. is not permitted in 0–25 GPa according to the comparison of enthalpy (Figure S9).[13,25] Since the structural changes of α-Sb_2O_3 are dominated by intermolecular van der Waals force, we first extracted intermolecular adjacent Sb–Sb, Sb–O, and O–O distances as a function of pressure, as presented in Figure 3b,c. Here the subscript numbers are used to distinguish different types of interatomic distances between Sb_4O_6 molecules. The structure illustrations of the two groups of Sb–Sb distance, three groups of Sb–O distance, and the O–O distance are displayed in Figures S10, S11, and S12, respectively. All these intermolecular atom distances mentioned above shorten fleetly in 0–4 GPa but shorten slowly in 4–25 GPa, which explains why the B_0 in 0–4 GPa is much smaller than those in 4–25 GPa.

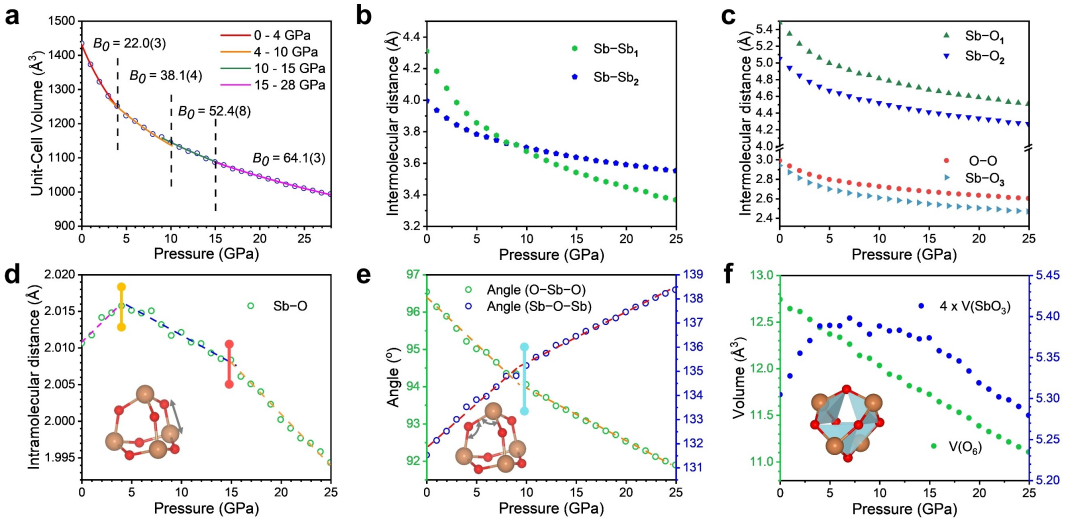

Figure 3. Simulated variations of crystal structure and molecular structure at high pressure. a) Pressure-dependent unit-cell volume of α-Sb_2O_3. b,c) Pressure-dependent interatomic distance of Sb–Sb, Sb–O, and O–O between the adjacent Sb_4O_6 molecules. d,e) Pressure dependence of the intramolecular Sb–O distance and the angle of O–Sb–O and Sb–O–Sb. f) Pressure dependence of the volume of the fourfold SbO_3 triangular pyramid and the O_6 regular octahedron.

The shortening of these intermolecular distances would inevitably affect the geometrical structure of the Sb_4O_6 molecule, i.e., the bond length and bond angle within the Sb_4O_6 molecule, as demonstrated in Figure 3d,e. The pressure coefficient of the Sb–O bond length shows two inflection points at 4 GPa and 15 GPa. Meanwhile, the pressure dependence of the Sb–O–Sb angle shows an inflection point at ~10 GPa. These three inflection points are close to the pressures where the pressure coefficient of E_g (120 cm^{-1}), A_g (255 cm^{-1}), and F_{2g} (362 cm^{-1}) modes change, strongly corroborating the three isostructural phase transitions. Moreover, softening (lengthening) of the intramolecular covalent bond is also revealed. The Sb–O bond length increases in 0–4 GPa and decreases in 4–25 GPa. The pressure dependence of Sb–O bond length is consistent with the molecular crystal vibrational model,[17a] which explains why the A_g mode (255 cm^{-1}) shows a red shift in 0–4 GPa but a blue shift in 4–22 GPa. The other two inflection points at 11 GPa and 16 GPa of the pressure dependence of A_g mode (255 cm^{-1}) in Figure 2d can be attributed to the changes of pressure dependence of the O–Sb–O angle at 10 GPa and Sb–O bond length at 15 GPa, respectively. In addition, lengthening of the Sb–O bond leads to the expansion of the SbO_3 triangular pyramid volume in 0–4 GPa (Figure 3f and Figure S13), which suggests that local structure in molecular crystals may expand during compression. Whereas its increase is negligible in comparison to the decrease of O_6 regular octahedron volume (Here the atoms are treated as particles), so the volume of the Sb_4O_6 molecule unit decreases monotonically in a nearly linear fashion (Figure S14). Through a detailed analysis of the displacements of Sb and O atoms upon compression (see supporting note 1 in the Supporting Information), we reveal that all the microscopic structural changes are triggered by the intermolecular repulsion of O–O, Sb–O_3, and Sb–Sb_1 atom pairs. These increased intermolecular repulsion forces with pressure would enhance intermolecular bonding, thus modifying the band structures and potentially improving the charge transport.[3,26]

In order to prove the changes in bonding properties during compression, the bond strength of the intramolecular Sb–O bond and the intermolecular adjacent atom pairs were quantified by bond order and electron localization function (ELF).[27] The bond orders are assessed by the density-derived electrostatic and chemical charge (DDEC) method.[28] A bond order value of "0" indicates pure ionic and a value of "1" reflects a full single covalent bond.[29] Similarly, the region with a high ELF value signifies the position of covalent bonding or lone-pair electrons (LPEs). ELF is a local measure of the effect of the Pauli repulsion on the kinetic energy density.[26c,30] The bond orders of different types of atom pairs in α-Sb_2O_3 at 0, 4, 10, and 15 GPa are summarized in Table S1. At ambient pressure, the bond order of the intramolecular Sb–O bond is 0.849 and it gradually decreases with the pressure increasing (Figure 4a). Conversely, the bond orders of the intermolec-

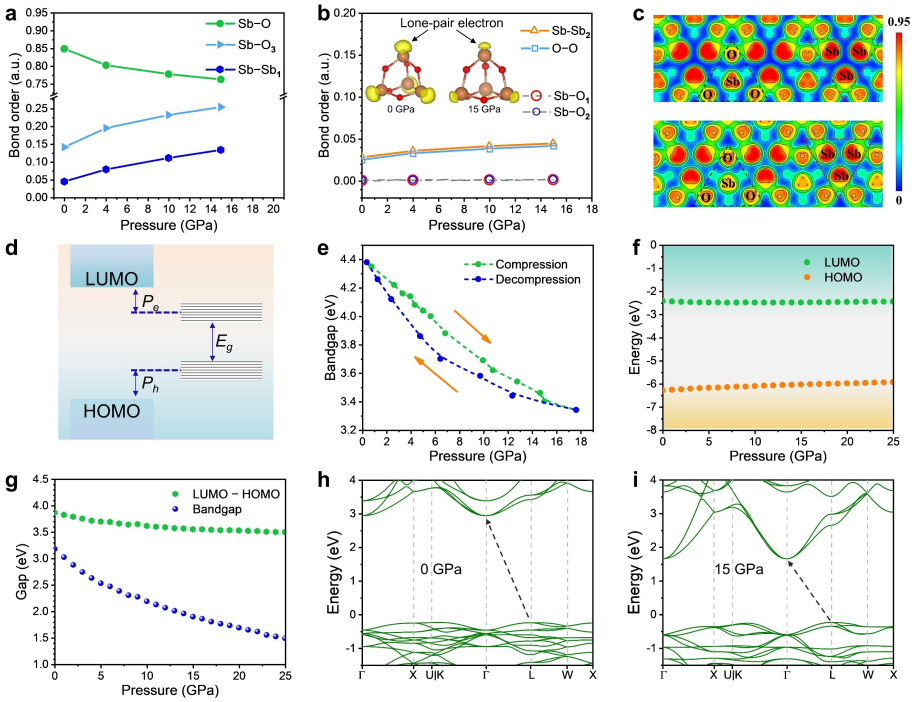

Figure 4. Pressure-induced variations of the bonding properties and band structure. a) Bond order evolution with pressure of the covalent Sb–O bond, and the intermolecular Sb–O_3 and Sb–Sb_1. b) Bond order evolutions of other intermolecular atom pairs. Inset, 3D ELF graphs of the Sb_4O_6 unit at 0 and 15 GPa. c) 2D ELF maps of α-Sb_2O_3 at 0 GPa (top) and 15 GPa (bottom) projected on the (111) plane. d) Schematic diagram of the energy levels for molecular crystals. e) The band gap evolution of an α-Sb_2O_3 flake during compression and decompression. f) Calculated LUMO and HOMO energy level positions of the Sb_4O_6 molecule. g) Calculated pressure dependences of the α-Sb_2O_3 band gap and the energy gap between LUMO and HOMO of the Sb_4O_6 molecule. h,i) Calculated band structures of α-Sb_2O_3 at 0 and 15 GPa.

ular Sb–O_3 and Sb–Sb_1 both increase significantly with pressure (Figure 4a), which implies enhanced intermolecular bonding. Nevertheless, the bond orders for other intermolecular atom pairs change very little with pressure (Figure 4b), suggesting that these interatomic forces play a small role in the structure transitions. In addition, all the bond orders for the aforementioned intermolecular atom pairs are still far below 0.5 at 15 GPa, meaning there is no formation of intermolecular covalent bonds. The enhancement of intermolecular bonding of Sb–O_3 and Sb–Sb_1 is further demonstrated by the 2D ELF maps (Figure 4c) and ELF line profiles (Figure S15), where the ELF values between Sb–O_3 and between Sb–Sb_1 in 15 GPa are larger than those in 0 GPa. The enhanced intermolecular bonding arises from the valence electron sharing between different atoms. Owing to the lone-pair electrons on the Sb atom being increasingly shared by the Sb and O atom on other surrounding molecules upon compression, the lobe-like charge extension of Sb $5s^2$ lone-pair electrons is suppressed significantly under high pressure, as demonstrated by the inset in Figure 4b.[19,26c]

The changes of intramolecular and intermolecular bonding properties and the Sb_4O_6 structure unit will highly regulate the band structure by changing the energy level positions of HOMO and LUMO of the Sb_4O_6 molecule, polarization energy (P_e and P_h), and band dispersion (Figure 4d).[31] The polarization energy and band dispersion are manifestations of intermolecular interactions.[31a,c] To explore the band gap variations of α-Sb_2O_3 flake, in situ pressure-dependent absorption spectra of the α-Sb_2O_3 flake were collected (Figure S16). The α-Sb_2O_3 band gaps at different pressures were estimated by extrapolating the linear portion of $(\alpha h\nu)^2$ versus $h\nu$.[14a] Figure 4e shows that the α-Sb_2O_3 band gap decreases from 4.4 eV to 3.3 eV monotonously with the increase of pressure and the process is reversible. Interestingly, though the Sb_4O_6 molecule structure indeed changes with pressure, the energy level positions of the lowest unoccupied molecular orbital (LUMO) and the highest occupied molecular orbital (HOMO) and the gap between them are extremely insensitive to the pressure (Figure 4f,g), which means the decrease of Sb_2O_3 band gap is dominated by the strengthening of intermolecular interaction that is mainly contributed by the enhancement of intermolecular Sb–O_3 and Sb–Sb_1 bonding (Figure 4a). In addition, the calculated band gap shows the same variation tendency as our experimental data To gain more insight into the electronic properties of α-Sb_2O_3, the band structures of α-Sb_2O_3 at the four representative pressures were calculated, as shown in Figure 4h,i and Figure S17. The corresponding DOS results are presented in Figure S18. The valence- and conduction-band edges are dominated by O *2p* and Sb *5p* states, respectively. Under higher pressure, the evolution of atomic orbital weights arises from hybridization between Sb *5s* and O *2p* electrons.[13a] As pressure increases, the nature of indirect-band-gap is maintained. The valence band maximum (VBM) and conduction band minimum (CBM) are located at *L*-point and *Γ*-point, respectively.

From the perspective of enhanced intermolecular bonding, the originally poor charge transport of 2D α-Sb_2O_3 flake may be greatly improved.[1b,3,26a] To investigate its electrical properties under high pressure, the resistivity of single-crystalline α-Sb_2O_3 flakes with different thicknesses was measured (Figure 5a). Au electrodes were coated (Figure S19) on the flakes and then connected with the Pt probes in the DAC chamber (Figure S20). At ambient pressure, the α-Sb_2O_3 flakes show insulating behavior with a high resistivity of about 10^8 Ω·m. During compression, the resistivity of these flakes decreases sharply by about 5 orders of magnitude within 0–3.2 GPa, while changes a little from 3.2 GPa to 18 GPa. Note that the onset pressure (Figure 5a) of the first isostructural phase transformation was postponed significantly with decreasing the thickness of α-Sb_2O_3 flakes (Figure 5b). According to Figure 5b, the critical thickness for the delayed effect on the onset pressure is estimated to be around 100 nm. This delay behavior arises from the interfacial adhesion force *f* between the mica substrate and α-Sb_2O_3 flake (Figure S21). The obstructive effect of the adhesion force *f* on in-plane compression is more significant for the thinner flakes, leading to the in-plane compression coefficient ε_{xy} of the thinner flake smaller than the bulk counterpart under the same pressure. To obtain the same in-plane compression, a larger pressure is needed for a thinner sample. Besides, the resistivity variations of α-Sb_2O_3 are nearly reversible during the compression-decompression cycle (Figure S22). Below the onset pressure of the first isostructural phase transformation, the steep decrease in resistivity can be attributed to the dramatically increased intermolecular charge transfer integral (Table S2) and the suppressed thermal vibration of Sb_4O_6 molecules,[3,6c,8] which

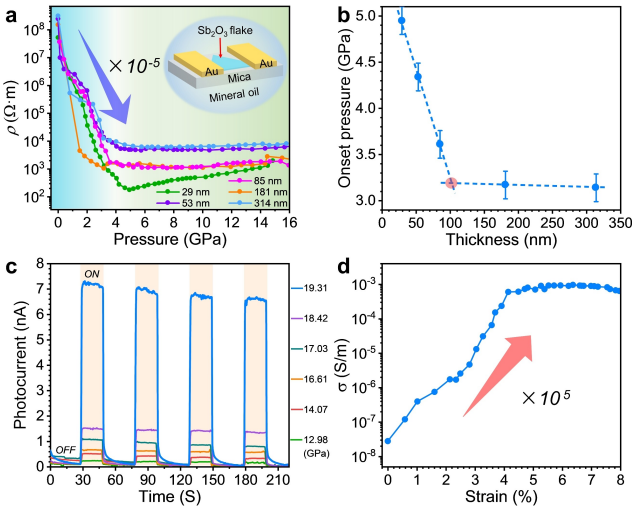

Figure 5. a) Pressure-dependent electrical resistivity of single-crystalline α-Sb_2O_3 flakes with different thicknesses. b) Thickness dependence of the onset pressure for the first isostructural phase transformation that was determined from Figure 5a. c) Photocurrents of the α-Sb_2O_3 flake with a thickness of 85 nm under different pressures. d) Conductivity for the flake with a thickness of 85 nm as a function of compressive strain of the lattice. The lattice parameters at different pressures were derived from unit-cell volume.

are incurred by the enhanced intermolecular Sb–O_3 and Sb–Sb_1 bonding. Above this pressure, the character of molecular crystal disappeared, as evidenced by the disappearance of the intermolecular vibration F_{2g} (84 cm^{-1}) mode over 3.77 GPa, which possibly changes the charge transport mechanism from hopping transport to band transport.[9b,32] Consequently, the nearly constant resistivity after the first isostructural transformation can be elucidated by the tiny change in the effective mass of electron and hole (Table S3 and S4) according to the band transport theory. Moreover, benefiting from the enhanced charge transport and reduced band gap, α-Sb_2O_3 flake exhibited gradually improved photoresponse after 13 GPa (Figure 5c and Figure S23). To further reveal the electro-mechanical response of α-Sb_2O_3 nanoflake, we plotted the conductivity of the device with a flake thickness of 85 nm as a function of lattice strain in Figure 5d. The dramatic increase of conductivity in 0–3.6 GPa is achieved within a strain of 4.1 %. Such a large electro-mechanical response is more sensitive than the state-of-the-art organic molecular crystal that was observed in TIPS-PEN (i.e., hole mobility increased by 20 times under a compressive strain of 16.7 %).[6b] Besides, the electro-mechanical response in α-Sb_2O_3 nanoflake is superior to those in common 2D materials.[33] To acquire a resistivity variation of 5 orders of magnitude, the pressures needed to apply on MoS_2, WS_2, $MoSe_2$, and $MoTe_2$ are 15 GPa,[20c] 25 GPa[34] 35 GPa,[35] and 15 GPa,[36] respectively. Importantly, the strain of 4.1 % is achievable for the flexible substrates.[6b,20a,b] Thus, the large increase of α-Sb_2O_3 conductivity in 0–3.6 GPa, from insulating to semiconducting, could inspire the designs of novel force-switching devices.

Conclusion

In conclusion, we have successfully prepared high-quality 2D α-Sb_2O_3 flakes using the VMS method and demonstrated the highly tunable charge transport in 2DIMCs by regulating the intermolecular interactions. Using in situ high-pressure Raman spectroscopy, we revealed three isostructural transformations at ~4 GPa, 10 GPa, and 15 GPa, respectively, correlating well with the microscopic structural changes on atomic level simulated by DFT. Meanwhile, the transition pressures of the isostructural transition can be further tailored by changing the sample thickness. The intermolecular bonding gradually strengthens with pressure but is free of forming covalent bonds up to 15 GPa, which plays a decisive role in the decrease of α-Sb_2O_3 band gap and the dramatic improvement of charge transport. Remarkably, a sharp decrease in resistivity by 5 orders of magnitude was observed in 0–3.2 GPa, which may have potential applications in switching devices. Our work not only reveals the variations of structure and intermolecular bonding in 2DIMCs on the atomic scale but also sheds light on the manipulation of charge transport in 2DIMCs, promising to advance the development of molecular physics and inspire their potential applications in optoelectronics and nano-electromechanical systems.

Acknowledgements

This work was supported by the National Natural Science Foundation of China (21825103, U21A2069). We also thank the technical support from the Analytical and Testing Center in Huazhong University of Science and Technology.

Conflict of Interest

The authors declare no conflict of interest.

Data Availability Statement

The data that support the findings of this study are available from the corresponding author upon reasonable request.

Keywords: 2D Inorganic Molecular Crystals · Charge Transport · High-Pressure · α-Sb_2O_3

[1] a) K. Liu, B. Jin, W. Han, X. Chen, P. Gong, L. Huang, Y. Zhao, L. Li, S. Yang, X. Hu, J. Duan, L. Liu, F. Wang, F. Zhuge, T. Zhai, *Nat. Electron.* **2021**, *4*, 906–913; b) W. Han, P. Huang, L. Li, F. Wang, P. Luo, K. Liu, X. Zhou, H. Li, X. Zhang, Y. Cui, T. Zhai, *Nat. Commun.* **2019**, *10*, 4728; c) X. Feng, X. Peng, B. Peng, Z. Li, W. Huang, S. Yang, K. Pei, Z. Sun, F. Huang, H. Li, Z. Shuai, T. Zhai, *J. Am. Chem. Soc.* **2021**, *143*, 20192–20201; d) L. Liu, P. Gong, K. Liu, A. Nie, Z. Liu, S. Yang, Y. Xu, T. Liu, Y. Zhao, L. Huang, H. Li, T. Zhai, *Adv. Mater.* **2022**, *34*, 2106041; e) K. Liu, L. Liu, T. Zhai, *J. Phys. Chem. Lett.* **2022**, *13*, 2173–2179.

[2] a) P. J. Reucroft, P. L. Kronick, H. Scott, M. M. Labes, *Nature* **1964**, *201*, 609–609; b) G. B. Street, W. D. Gill, *Phys. Status Solidi B* **1966**, *18*, 601–607; c) W. E. Spear, *Appl. Opt.* **1969**, *8*, 8–14; d) J. M. Caywood, C. A. Mead, *J. Phys. Chem. Solids* **1970**, *31*, 983–994; e) A. R. Adams, W. E. Spear, *J. Phys. Chem. Solids* **1964**, *25*, 1113–1118.

[3] A. Landi, A. Peluso, A. Troisi, *Adv. Mater.* **2021**, *33*, 2008049.

[4] a) G. Giri, E. Verploegen, S. C. Mannsfeld, S. Atahan-Evrenk, D. H. Kim, S. Y. Lee, H. A. Becerril, A. Aspuru-Guzik, M. F. Toney, Z. Bao, *Nature* **2011**, *480*, 504–508; b) S. Huang, G. Zhang, F. Fan, C. Song, F. Wang, Q. Xing, C. Wang, H. Wu, H. Yan, *Nat. Commun.* **2019**, *10*, 2447; c) F. Bai, K. Bian, X. Huang, Z. Wang, H. Fan, *Chem. Rev.* **2019**, *119*, 7673–7717.

[5] a) S. B. Desai, G. Seol, J. S. Kang, H. Fang, C. Battaglia, R. Kapadia, J. W. Ager, J. Guo, A. Javey, *Nano Lett.* **2014**, *14*, 4592–4597; b) C. He, R. Wu, L. Zhu, Y. Huang, W. Du, M. Qi, Y. Zhou, Q. Zhao, X. Xu, *J. Phys. Chem. Lett.* **2022**, *13*, 352–361; c) S. Yang, Y. Chen, C. Jiang, *InfoMat* **2021**, *3*, 397–420; d) X. Lu, C. Stoumpos, Q. Hu, X. Ma, D. Zhang, S. Guo, J. Hoffman, K. Bu, X. Guo, Y. Wang, C. Ji, H. Chen, H. Xu, Q. Jia, W. Yang, M. G. Kanatzidis, H. K. Mao, *Natl. Sci. Rev.* **2021**, *8*, nwaa288.

[6] a) H. H. Choi, H. T. Yi, J. Tsurumi, J. J. Kim, A. L. Briseno, S. Watanabe, J. Takeya, K. Cho, V. Podzorov, *Adv. Sci.* **2020**, *7*, 1901824; b) Y. Park, K. S. Park, B. Jun, Y.-E. K. Lee, S. U. Lee, M. M. Sung, *Chem. Mater.* **2017**, *29*, 4072–4079; c) T. Kubo, R. Hausermann, J. Tsurumi, J. Soeda, Y. Okada, Y. Yamashita, N. Akamatsu, A. Shishido, C. Mitsui, T. Okamoto, S. Yanagisawa, H. Matsui, J. Takeya, *Nat. Commun.* **2016**, *7*, 11156.

[7] a) Y. Wang, L. Sun, C. Wang, F. Yang, X. Ren, X. Zhang, H. Dong, W. Hu, *Chem. Soc. Rev.* **2019**, *48*, 1492–1530; b) L. Zhang, M. Mehedi Hasan, Y. Tang, A. Raza Khan, H. Yan, T. Yildirim, X. Sun, J. Zhang, J. Zhu, Y. Zhang, Y. Lu, *Mater. Today* **2021**, *50*, 442–475.
[8] S. Fratini, M. Nikolka, A. Salleo, G. Schweicher, H. Sirringhaus, *Nat. Mater.* **2020**, *19*, 491–502.
[9] a) S. Fratini, S. Ciuchi, D. Mayou, G. T. de Laissardiere, A. Troisi, *Nat. Mater.* **2017**, *16*, 998–1002; b) W. Li, J. Ren, Z. Shuai, *Nat. Commun.* **2021**, *12*, 4260.
[10] A. Grzechnik, *J. Solid State Chem.* **1999**, *144*, 416–422.
[11] S. J. Gilliam, J. O. Jensen, A. Banerjee, D. Zeroka, S. J. Kirkby, C. N. Merrow, *Spectrochim. Acta Part A* **2004**, *60*, 425–434.
[12] a) K. Yang, T. Zhang, B. Wei, Y. Bai, S. Jia, G. Cao, R. Jiang, C. Zhang, E. Gao, X. Chang, J. Li, S. Li, D. Zhu, R. Tai, H. Zhou, J. Wang, M. Zeng, Z. Wang, L. Fu, *Nat. Commun.* **2020**, *11*, 2502; b) K. Ye, L. Liu, J. Huang, A. Nie, K. Zhai, B. Wang, F. Wen, C. Mu, Z. Zhao, Y. Gong, J. Xiang, Y. Tian, Z. Liu, *Adv. Opt. Mater.* **2020**, *8*, 2000168.
[13] a) A. L. J. Pereira, L. Gracia, D. Santamaría-Pérez, R. Vilaplana, F. J. Manjón, D. Errandonea, M. Nalin, A. Beltrán, *Phys. Rev. B* **2012**, *85*, 174108; b) Z. Zhao, Q. Zeng, H. Zhang, S. Wang, S. Hirai, Z. Zeng, W. L. Mao, *Phys. Rev. B* **2015**, *91*, 184112.
[14] a) J. Peng, W. Pu, S. Lu, X. Yang, C. Wu, N. Wu, Z. Sun, H. T. Wang, *Nano Lett.* **2021**, *21*, 203–208; b) C. Wu, J. Peng, W. Pu, S. Lu, C. Zhang, N. Wu, Z. Sun, H. Zhang, H. T. Wang, *J. Phys. Chem. Lett.* **2021**, *12*, 9011–9019.
[15] a) S. Guo, K. Bu, J. Li, Q. Hu, H. Luo, Y. He, Y. Wu, D. Zhang, Y. Zhao, W. Yang, M. G. Kanatzidis, X. Lu, *J. Am. Chem. Soc.* **2021**, *143*, 2545–2551; b) K. Bu, Q. Hu, X. Qi, D. Wang, S. Guo, H. Luo, T. Lin, X. Guo, Q. Zeng, Y. Ding, F. Huang, W. Yang, H. K. Mao, X. Lu, *Nat. Commun.* **2022**, *13*, 4650; c) S. Guo, Y. Li, Y. Mao, W. Tao, K. Bu, T. Fu, C. Zhao, H. Luo, Q. Hu, H. Zhu, E. Shi, W. Yang, L. Dou, X. Lu, *Sci. Adv.* **2022**, *8*, eadd1984.
[16] Q. Li, Y. Wang, W. Pan, W. Yang, B. Zou, J. Tang, Z. Quan, *Angew. Chem. Int. Ed. Angew. Chem. Int. Ed. Engl.* **2017**, *56*, 15969–15973.
[17] a) R. Zallen, *Phys. Rev. B* **1974**, *9*, 4485–4496; b) R. Zallen, M. L. Slade, *Phys. Rev. B* **1978**, *18*, 5775–5798; c) G. R. Burns, J. R. Rollo, *J. Phys. Chem. Solids* **1987**, *48*, 347–354.
[18] G. A. Kourouklis, E. Anastassakis, *Phys. Rev. B* **1986**, *34*, 1233–1237.
[19] K. Bu, H. Luo, S. Guo, M. Li, D. Wang, H. Dong, Y. Ding, W. Yang, X. Lu, *J. Phys. Chem. Lett.* **2020**, *11*, 9702–9707.
[20] a) H. J. Conley, B. Wang, J. I. Ziegler, R. F. Haglund Jr., S. T. Pantelides, K. I. Bolotin, *Nano Lett.* **2013**, *13*, 3626–3630; b) Z. Li, Y. Lv, L. Ren, J. Li, L. Kong, Y. Zeng, Q. Tao, R. Wu, H. Ma, B. Zhao, D. Wang, W. Dang, K. Chen, L. Liao, X. Duan, X. Duan, Y. Liu, *Nat. Commun.* **2020**, *11*, 1151; c) A. P. Nayak, S. Bhattacharyya, J. Zhu, J. Liu, X. Wu, T. Pandey, C. Jin, A. K. Singh, D. Akinwande, J. F. Lin, *Nat. Commun.* **2014**, *5*, 3731.
[21] R. M. Hazen, W. F. Larry, *Sci. Am.* **1985**, *252*, 110–117.
[22] a) R. S. Alencar, K. D. A. Saboia, D. Machon, G. Montagnac, V. Meunier, O. P. Ferreira, A. San-Miguel, A. G. Souza Filho, *Phys. Rev. Mater.* **2017**, *1*, 024002; b) K. Filintoglou, N. Papadopoulos, J. Arvanitidis, D. Christofilos, O. Frank, M. Kalbac, J. Parthenios, G. Kalosakas, C. Galiotis, K. Papagelis, *Phys. Rev. B* **2013**, *88*, 045418; c) Z. Wang, O. Chen, C. Y. Cao, K. Finkelstein, D. M. Smilgies, X. Lu, W. A. Bassett, *Rev. Sci. Instrum.* **2010**, *81*, 093902; d) Z. Wang, C. Schliehe, T. Wang, Y. Nagaoka, Y. C. Cao, W. A. Bassett, H. Wu, H. Fan, H. Weller, *J. Am. Chem. Soc.* **2011**, *133*, 14484–14487.
[23] a) N. P. Salke, K. Xia, S. Fu, Y. Zhang, E. Greenberg, V. B. Prakapenka, J. Liu, J. Sun, J. F. Lin, *Phys. Rev. Lett.* **2021**, *126*, 065702; b) T. Lüdtke, D. Wiedemann, I. Efthimiopoulos, N. Becker, S. Seidel, O. Janka, R. Pottgen, R. Dronskowski, M. Koch-Muller, M. Lerch, *Inorg. Chem.* **2017**, *56*, 2321–2327; c) S. Grimme, J. Antony, S. Ehrlich, H. Krieg, *J. Chem. Phys.* **2010**, *132*, 154104.
[24] F. Birch, *Phys. Rev.* **1947**, *71*, 809–824.
[25] J. R. Nelson, R. J. Needs, C. J. Pickard, *Phys. Rev. B* **2017**, *95*, 054118.
[26] a) X. Cui, D. Han, H. Guo, L. Zhou, J. Qiao, Q. Liu, Z. Cui, Y. Li, C. Lin, L. Cao, W. Ji, H. Petek, M. Feng, *Nat. Commun.* **2019**, *10*, 3374; b) M. Shaikh, S. Ghosh, S. Ghosh, *Mater. Lett.* **2021**, *304*, 130590; c) P. Wang, Y. Wang, J. Qu, Q. Zhu, W. Yang, J. Zhu, L. Wang, W. Zhang, D. He, Y. Zhao, *Phys. Rev. B* **2018**, *97*, 235202.
[27] a) T. A. Manz, D. S. Sholl, *J. Chem. Theory Comput.* **2012**, *8*, 2844–2867; b) B. Silvi, A. Savin, *Nature* **1994**, *371*, 683–686; c) A. Savin, B. Silvi, F. Colonna, *Can. J. Chem.* **1996**, *74*, 1088–1096.
[28] a) T. A. Manz, N. G. Limas, *RSC Adv.* **2016**, *6*, 47771–47801; b) N. G. Limas, T. A. Manz, *RSC Adv.* **2016**, *6*, 45727–45747; c) T. A. Manz, *RSC Adv.* **2017**, *7*, 45552–45581; d) N. G. Limas, T. A. Manz, *RSC Adv.* **2018**, *8*, 2678–2707.
[29] W. Lai, Y. Wang, D. T. Morelli, X. Lu, *Adv. Funct. Mater.* **2015**, *25*, 3648–3657.
[30] a) A. Savin, R. Nesper, S. Wengert, T. F. Fässler, *Angew. Chem. Int. Ed. Engl.* **1997**, *36*, 1808–1832; *Angew. Chem.* **1997**, *109*, 1892–1918; b) M. Kohout, F. R. Wagner, Y. Grin, *Theor. Chem. Acc.* **2002**, *108*, 150–156.
[31] a) K. Yamada, S. Yanagisawa, T. Koganezawa, K. Mase, N. Sato, H. Yoshida, *Phys. Rev. B* **2018**, *97*, 245206; b) M. Yu, X. Wang, X.-F. Du, C. Kunkel, T. M. Garcia, S. Monaco, B. Schatschneider, H. Oberhofer, N. Marom, *Synth. Met.* **2019**, *253*, 9–19; c) F. Brown-Altvater, G. Antonius, T. Rangel, M. Giantomassi, C. Draxl, X. Gonze, S. G. Louie, J. B. Neaton, *Phys. Rev. B* **2020**, *101*, 165102.
[32] a) G. Schweicher, G. D'Avino, M. T. Ruggiero, D. J. Harkin, K. Broch, D. Venkateshvaran, G. Liu, A. Richard, C. Ruzie, J. Armstrong, A. R. Kennedy, K. Shankland, K. Takimiya, Y. H. Geerts, J. A. Zeitler, S. Fratini, H. Sirringhaus, *Adv. Mater.* **2019**, *31*, 1902407; b) H. Oberhofer, K. Reuter, J. Blumberger, *Chem. Rev.* **2017**, *117*, 10319–10357.
[33] L. Zhang, Y. Tang, A. R. Khan, M. M. Hasan, P. Wang, H. Yan, T. Yildirim, J. F. Torres, G. P. Neupane, Y. Zhang, Q. Li, Y. Lu, *Adv. Sci.* **2020**, *7*, 2002697.
[34] A. P. Nayak, Z. Yuan, B. Cao, J. Liu, J. Wu, S. T. Moran, T. Li, D. Akinwande, C. Jin, J. F. Lin, *ACS Nano* **2015**, *9*, 9117–9123.
[35] Z. Zhao, H. Zhang, H. Yuan, S. Wang, Y. Lin, Q. Zeng, G. Xu, Z. Liu, G. K. Solanki, K. D. Patel, Y. Cui, H. Y. Hwang, W. L. Mao, *Nat. Commun.* **2015**, *6*, 7312.
[36] L. Yang, L. Dai, H. Li, H. Hu, K. Liu, C. Pu, M. Hong, P. Liu, *AIP Adv.* **2019**, *9*, 065104.

Manuscript received: November 23, 2022
Accepted manuscript online: December 3, 2022
Version of record online: ■■, ■■

Research Articles

Charge Transport

X. Feng, K. Bu, T. Liu, S. Guo, Z. Sun, T. Fu, Y. Xu, K. Liu, S. Yang, Y. Zhao, H. Li, L. Lü,* T. Zhai* _____ **e202217238**

Giant Tunability of Charge Transport in 2D Inorganic Molecular Crystals by Pressure Engineering

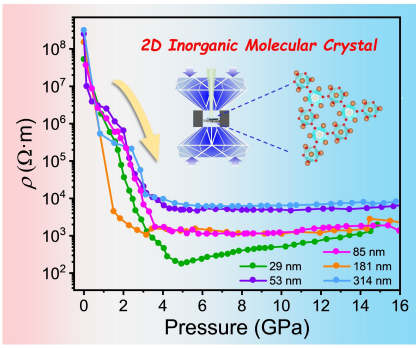

Giant tunability of charge transport in two-dimensional inorganic molecular crystals, from an insulator to a semiconductor, is revealed for the first time through in situ high-pressure experimental characterizations.